

Manuscript version: Author's Accepted Manuscript

The version presented in WRAP is the author's accepted manuscript and may differ from the published version or Version of Record.

Persistent WRAP URL:

<http://wrap.warwick.ac.uk/160185>

How to cite:

Please refer to published version for the most recent bibliographic citation information. If a published version is known of, the repository item page linked to above, will contain details on accessing it.

Copyright and reuse:

The Warwick Research Archive Portal (WRAP) makes this work by researchers of the University of Warwick available open access under the following conditions.

© 2021 Elsevier. Licensed under the Creative Commons Attribution-NonCommercial-NoDerivatives 4.0 International <http://creativecommons.org/licenses/by-nc-nd/4.0/>.



Publisher's statement:

Please refer to the repository item page, publisher's statement section, for further information.

For more information, please contact the WRAP Team at: wrap@warwick.ac.uk.

Swelling and embedment induced by sub- and super-critical-CO₂ on the permeability of propped fractures in shale

Lei Hou ^{a,*}, Derek Elsworth ^{b,*}, Xueyu Geng ^a

^a School of Engineering, The University of Warwick, Coventry CV4 7AL, UK

^b Energy and Mineral Engineering, EMS Energy Institute and G3 Center, Pennsylvania State University, University Park, 16802, USA

Abstract

Swelling and embedment exert significant influence on the evolution of permeability in propped fractures, potentially consuming significant proportions of the original gain in permeability. We measure the evolution of permeability in propped fractures of shale to both adsorbing CO₂ and non-adsorbing He – accommodating the impacts of aperture change due to proppant pack compaction and both reversible and irreversible modes of embedment. A linear relation between pressure and log-permeability is obtained for He, representing the impact of effective stresses in proppant pack compaction, alone. Permeability change with pressure is always concave upwards and U-shaped for gaseous subcritical CO₂ and W-shaped for supercritical CO₂. One exception is for liquid CO₂ at high injection pressure where effective stress effects and swelling contribute equally to the change in permeability and result in a linear curve with the lowest permeability. Approximately ~50-70 % of the permeability recovers from the recovery of swelling after the desorption of CO₂. The magnitude of swelling is recovered from measurements of permeability change and ranges from 0.005 to 0.06 mm, which contributes ~9-56 % of the total swelling and induced embedment as evaluated from the adsorbed mass. Swelling also increases embedment by a factor of ~1.84-1.93 before and after the injection of CO₂. A new calibration equation representing swelling and induced embedment is generated accommodating Langmuir isothermal sorption and verified against experiments on rocks both admitting and excluding swelling and embedment and for various sorbing and non-sorbing gases. Stability and accuracy of the predictions demonstrate the universality of the approach that may be applied to both enhanced gas recovery and CO₂ sequestration.

Keywords: swelling, embedment, propped shale fracture, permeability, carbon dioxide

* Corresponding authors.

E-mail address: lei.hou@warwick.ac.uk (L. Hou), elsworth@psu.edu (D. Elsworth)

1 Introduction

2 CO₂ applications have a long history in the energy industries including for EOR (Enhanced Oil
3 Recovery) (Kolster, Masnadi, Krevor, Mac Dowell, & Brandt, 2017; Sen Wang, Feng, Javadpour,
4 Xia, & Li, 2015), CO₂ fracturing (H. Liu, Wang, Zhang, Meng, & Duan, 2014; Middleton et al., 2015;
5 Xinwei Zhang, Lu, Tang, Zhou, & Liao, 2017) and for storage in saline aquifers and depleted
6 reservoirs (Bielicki et al., 2018; Buscheck, White, Carroll, Bielicki, & Aines, 2016; Tayari &
7 Blumsack, 2020). As a strongly adsorbing gas, permeability evolution involving swelling and fracture
8 closure is one essential issue. Sorbing CO₂ swells the rock matrix and causes a reduction in the natural
9 fracture aperture (H.-H. Liu & Rutqvist, 2009; Mazumder & Wolf, 2008; Xiaogang Zhang, Ranjith,
10 Lu, & Ranathunga, 2019). This swelling behaviour follows the Langmuir isotherm and reaches
11 maximum influence at approximately twice the Langmuir pressure (Shugang Wang, Elsworth, & Liu,
12 2011). The competition between swelling and effective stress results in a typical U-shaped curve for
13 permeability as a function of increasing gas pressure for both integral and split samples (Kumar,
14 Elsworth, Liu, Pone, & Mathews, 2015; Shugang Wang, Elsworth, & Liu, 2013). Where the fluid is
15 supercritical, a W-shaped curve may additionally result (Zhi, Elsworth, & Liu, 2019).

16 An accompanying issue with a similar significant impact on permeability is that of particle
17 embedment in propped fractures - occurring when the particle has a higher stiffness than the rock. The
18 embedment, by itself, may induce a 10 to 60 % reduction in fracture aperture with a subsequent
19 significant (78 %) loss in conductivity in shale (Bandara, Ranjith, & Rathnaweera, 2019; Santos, Dahi
20 Taleghani, & Li, 2018; Jingchen Zhang & Hou, 2016). Prior characterizations have examined the
21 roles of mineral composition (clay content), mechanical properties, interaction between the rock
22 surface and the fracturing fluid, closure stress, proppant concentration and formation temperature and
23 pressure in modulating response (Arshadi, Zolfaghari, Piri, Al-Muntasheri, & Sayed, 2017; Tang &
24 Ranjith, 2018; Wen, Zhang, Wang, Liu, & Li, 2007; Junjing Zhang, Ouyang, Zhu, & Hill, 2015).
25 Swelling is relatively less important for shales, relative to coals, because of their lower organic
26 contents and higher stiffnesses. However, conventional methods of characterization applied in former
27 studies are incapable of distinguishing between swelling and embedment under either static loading or

28 API (American Petroleum Institute) standard conductivity tests. Associated with swelling, embedment
29 is accentuated in rocks of low modulus. Recent studies have demonstrated the significant effect of
30 swelling on permeability evolution in propped fractures in shale which are also shown to result in
31 typical U-shaped curves of permeability with pressure (Li et al., 2017).

32 Nonetheless, the behaviour of swelling and induced embedment, and their respective contribution
33 to the destruction of permeability in propped fractures, is poorly defined since the direct observation
34 of swelling is infeasible in real-time and under triaxially stressed, sealed and gas injection conditions.
35 Therefore, we explore the impacts of swelling-induced embedment of proppant in artificial fluid-
36 driven fractures. We measure permeability loss with the injection of both non-adsorptive Helium (He)
37 and adsorptive carbon dioxide (CO₂) on samples of Green River shale to (i) quantitatively reveal the
38 respective roles of swelling and embedment, (ii) define the different controlling mechanisms of
39 permeability evolution, and (iii) define a model for embedment that accommodates the influence of
40 swelling that provides a better prediction of fracture conductivity and understanding of gas production
41 and CO₂ sequestration.

42 **2 Methodology**

43 We measure permeability evolution to CO₂ and He in propped fractures in both shale (that
44 accommodates embedment and swelling) and granite (that excludes these effects) *via* pressure
45 transient (pulse) methods. The apparatus (core holder and reservoirs) is immersed within a
46 temperature-controlled water bath to control the state of CO₂, as either sub- or super-critical. We
47 measure permeability to CO₂ and He alternately in the same sample. Based on the outcomes, we
48 define controlling mechanisms on the evolution of embedment and their impact on permeability.

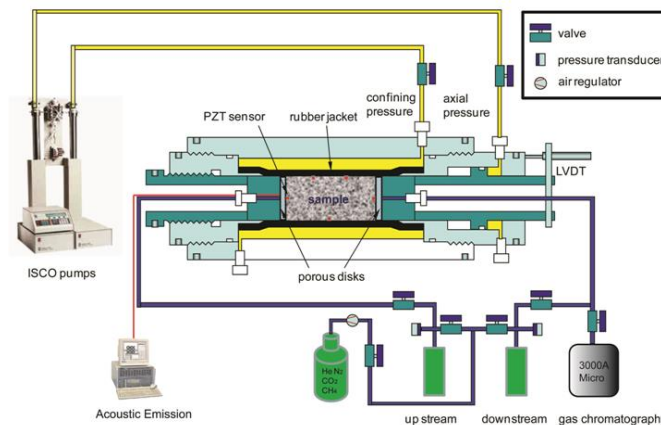
49 **2.1 Materials and preparation**

50 Axially-split core samples (25mm diameter 50mm length) of Westerly granite and Green River
51 shale are placed in a pressurized core holder with proppant sandwiched within the fracture. The high
52 strength Carbo-Lite ceramic proppant is segregated by size fraction (40/80 mesh). A single layer of
53 proppant is first sandwiched between the two facing artificial fractures. In particular, we explore the
54 behaviour of a monolayer since the deformation of proppant can be calculated more accurately, and

55 leaves swelling and embedment as the main factors influencing permeability evolution. The
 56 proportion of monolayer-propped fractures in field-fracturing is significant. This is apparent in branch
 57 fractures or micro-fractures and composes a crucial amount of the total stimulated reservoir volume
 58 (Gale, Laubach, Olson, Eichhuble, & Fall, 2014; Hoek & Martin, 2014; Weng, 2015). We use sorbing
 59 CO₂ (purity of 99.995 %) and effectively- non-sorbing He (99.999 %) as contrasting permeants for the
 60 permeability measurement.

61 **2.2 Apparatus**

62 A standard triaxial apparatus, as shown in Fig. 1, is used as the pressurized core holder. The
 63 proppant-sandwiching sample is packed with tape then jacketed in a Viton rubber jacket to seal and
 64 isolate the sample from the confining fluid in the core holder. This assembly is then placed in the
 65 triaxial core holder (Temco) where both confining and axial stresses to 25 MPa are applied by syringe
 66 pumps (ISCO 500D) to a resolution of ± 0.007 MPa. The axial stress is transmitted directly onto both
 67 ends of the sample through the platens which connect flow lines to fluid distributors. The end-platens
 68 are plumbed to two stainless steel gas reservoirs through tubing and isolating valves at both upstream
 69 and downstream extents of the sample. Reservoir volumes are 26.7 ml for the upstream and 16.8 ml
 70 for the downstream with reservoir pressures measured by transducers (Omega PX302-2KGV and
 71 Omega PX302-5KGV) to resolutions of ± 0.03 MPa. Each transducer is calibrated for each new
 72 sample with National Instruments Labview used for data acquisition and pump control.

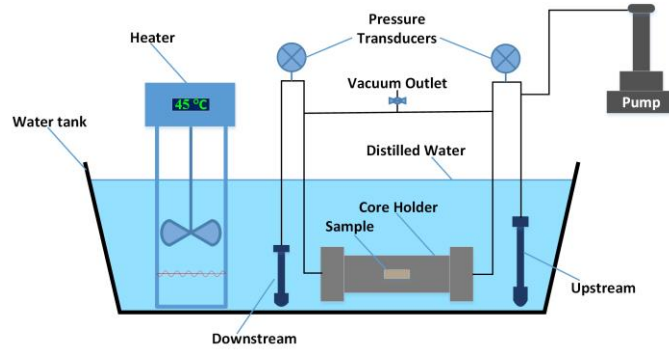


73
 74 **Fig. 1. Schematic of the experimental apparatus (Wang, Elsworth, & Liu, 2011).**

75 **2.3 Procedure**

76 We use standard pressure transient (pulse) methods for permeability measurements. Once the
 77 sample is in the core holder, the system is first evacuated for one hour and then saturated with the

78 desired gas (CO₂ or He). Then, a pressure difference (pulse) is applied between upstream and
 79 downstream and its upstream decay and downstream build-up behaviour is recorded and analysed to
 80 obtain the permeability (Shugang Wang et al., 2011). The tests are performed at both room
 81 temperature (23 °C) and supercritical temperature (45 °C) in a water bath, as shown in Fig. 2. Interior
 82 gas pressures in the range 2 to 13 MPa access the various phase states of CO₂.



83
84 **Fig. 2. Schematic of water tank heating system.**

85 We measure the permeabilities alternately with CO₂ and then He in the same sample to evaluate
 86 the impact of the gas on permeability and its recovery/loss after swelling. Then, a comprehensive
 87 analysis is performed for the quantitative description of swelling and embedment. As a part of the
 88 standard pulse decay method, the permeability is calculated as (Brace, Walsh, & Frangos, 1968),

89
$$k = \frac{\alpha \mu \beta L V_{up} V_{dn}}{A(V_{up} + V_{dn})} \quad (1)$$

90 where α is the slope of pressure decay against the logarithm of time; μ and β are the viscosity and
 91 compressibility of the fluid, respectively; L is the length of the sample; V_{up} and V_{dn} are volumes of the
 92 upstream and downstream reservoirs, respectively; and A is the fluid flow cross-section area in
 93 fracture (permeation through the rock matrix is ignored).

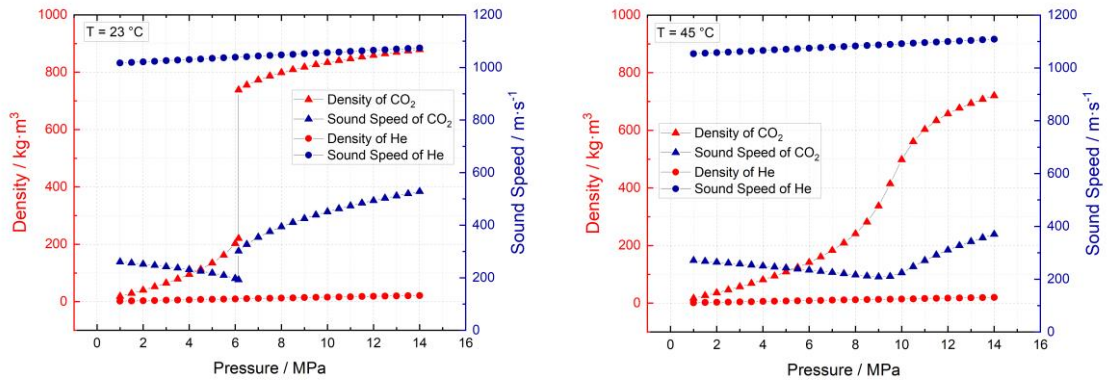
94 The cross-sectional area A is calculated from the average particle diameter and is considered
 95 constant for all testing samples. The compressibility of the fluid β is calculated from the bulk modulus

96
$$\beta = \frac{1}{B_M} = \frac{1}{v^2 \rho} \quad (2)$$

97 where B_M is the bulk modulus of the fluid; v is the speed of sound in the fluid; and ρ is the fluid
 98 density.

99 The values of v and ρ are recovered from standard characterizations (National Institute of
 100 Standards and Technology (NIST)), as shown in Fig. 3. The density and speed of sound in He

101 increase linearly versus pressure with small slopes, although those properties for CO₂ increase or
 102 decrease gradually then jump or fall sharply around the phase change pressure. The properties of CO₂
 103 then vary more continuously with pressure at 45 °C than those at 23 °C. Both decline at high
 104 temperature, especially under high pressure.



105
 106 **Fig. 3. Density and speed of sound in CO₂ and He (NIST database).**

107 **3 Results**

108 A total of five groups of permeability measurements are conducted with multiple repeats in each of
 109 these five groups. Each probing injection (increasing gas pressure) and depletion (decreasing gas
 110 pressure) are repeated at least three times. The measurements are for CO₂ as gaseous, liquid then
 111 supercritical states. The permeabilities for the granite sample are used as a reference where neither
 112 embedment nor swelling may occur. Shale sample A was used for multi-purpose testing with repeat
 113 tests with He used on samples B, C and D to measure the permeability recovery after CO₂-induced
 114 swelling and corresponding embedment. The experimental matrix is shown in Table 1.

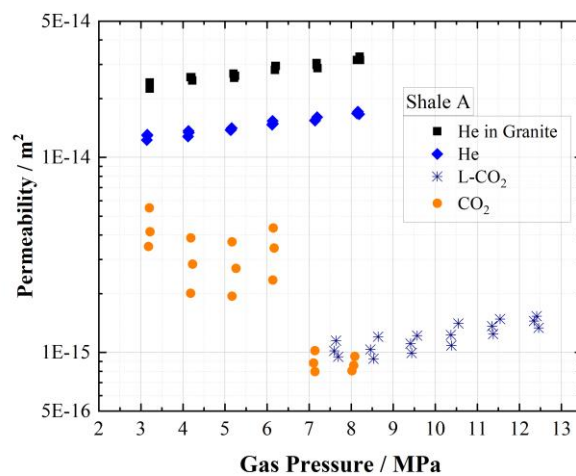
115 **Table 1. Matrix of experiments defining samples and conditions.**

Sample Type & No.	Westerly Granite	Greenriver Shale			
		A	B	C	D
Dimensions	25 * 50 mm				
Proppant	Carbo-Lite Ceramisite; 40/80 Mesh (D = 0.177 ~ 0.400 mm)				
Gas	Helium	Helium & Carbon Dioxide			
Confining & Axial Pressure	25 MPa				
Injection Pressure	3 ~ 9 MPa	3 ~ 13 MPa	2 ~ 9 MPa	2 ~ 13 MPa	2 ~ 10 MPa
Temperature	23 °C				45 °C

116 **3.1 General testing results**

117 Permeability evolutions in granite and shale (sample A) are shown in Fig. 4. Generally, the granite
 118 has the largest permeability followed by the “shale + He” case, in which approximately half of the
 119 permeability is consumed by the embedment. The lowest permeability is obtained for the case of
 120 liquid CO₂. Positive linear relationships between increasing gas pressure and increasing permeability
 121 are found in those cases.

122 Swelling and more significant corresponding embedment diminish the permeability significantly
 123 for infiltration with gaseous CO₂. A typical U-shaped curve results due to the competition between
 124 adsorption (low pressure limit) and effective stress (high gas pressure limit). The permeability relation
 125 is a minimum at approximately double the Langmuir pressure of ~5 MPa in this case. The dramatic
 126 drop at ~7 MPa has been explained by the sudden volume change during the phase transition of the
 127 CO₂ for a relatively stable pressure (Li et al., 2017). For both gaseous and liquid CO₂, the
 128 permeabilities remain continuous for overlapping pressures in the range ~7 to 9 MPa.



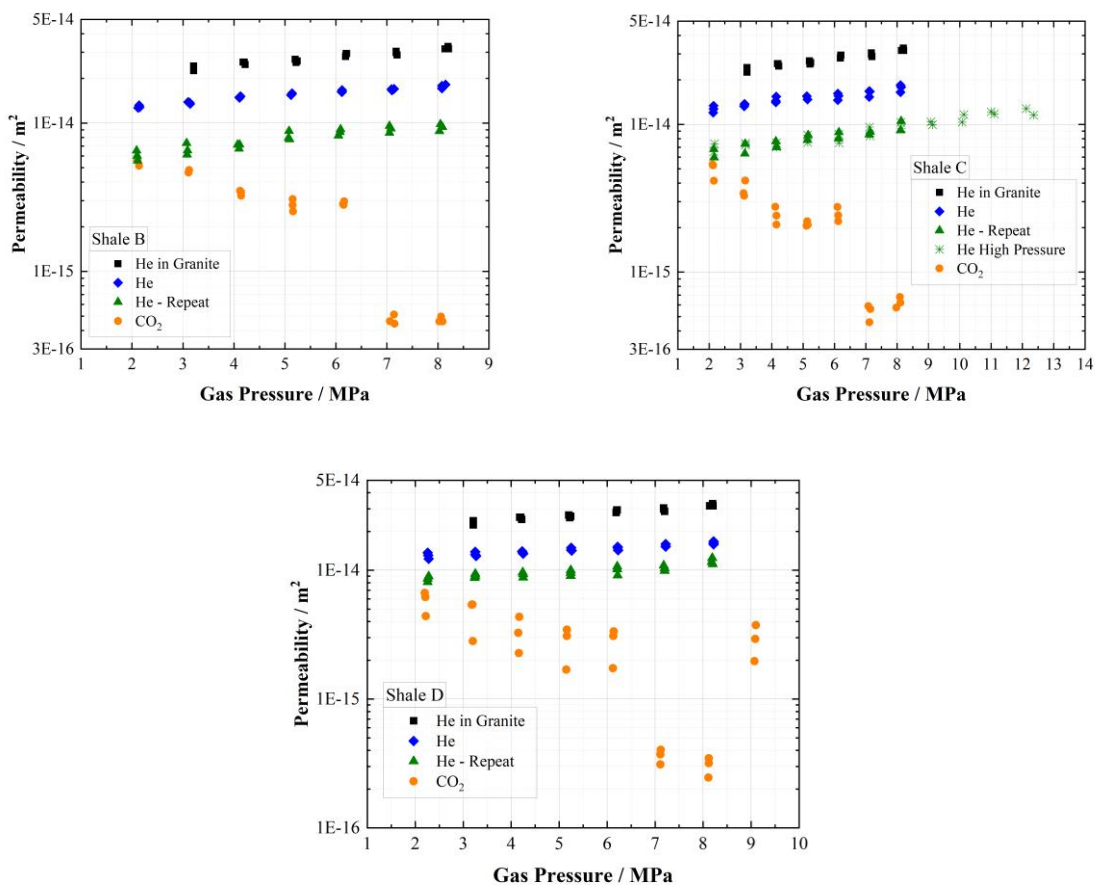
129
 130 **Fig. 4. Permeability evolution versus gas pressure in granite and in shale sample A with injection of He, CO₂**
 131 **(gaseous) and liquid CO₂ (L-CO₂). The temperature is 23 °C.**

132 **3.2 Permeability recovery behaviour**

133 Repeat experiments on shale samples B, C and D reveal the permeability recovery behaviour
 134 following swelling. The permeability returns to ~50 to 70 % of the initial value in the repeated He test
 135 after injecting CO₂ and shows a parallel linear trend with the prior measurements, as shown in Fig. 5.
 136 It is worth noting that the recovery period is relatively short. A comparative trial over different

137 recovery periods (hours and days) yielded similar results. In these tests, the system is evacuated for at
 138 least one hour to ensure the complete recovery of swelling.

139 The three separate groups of the experiments present relatively good repeatability in both values of
 140 permeability and trends with pressure and gas state. A minor difference in the repeated He
 141 permeability measurement is found in sample D, where the operating temperature is 45 °C and CO₂
 142 exists in a supercritical state. Nearly 70 % of the permeability is restored, an increase of ~20 % when
 143 compared with the cases for gaseous CO₂. Moreover, a W-shaped curve is apparent for supercritical
 144 CO₂, which is in accordance with observations on intact specimens of coal (Zhi et al., 2019) -
 145 explained by the synthetic effect of phase transition around the critical point and the plasticization of
 146 the solid material by supercritical CO₂.

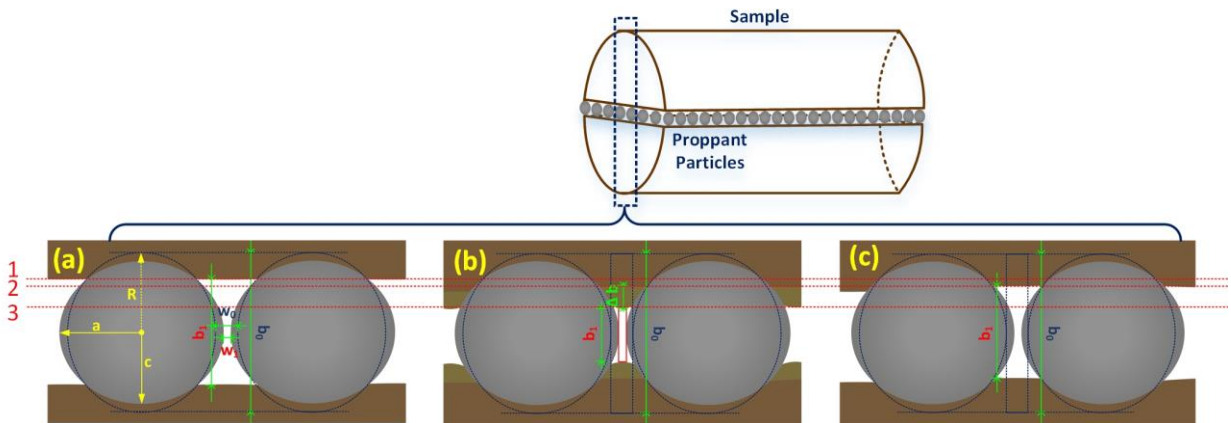


147

148 **Fig. 5. Permeability evolution in samples B, C and D. The experimental temperatures are 23 °C for samples B and C**
 149 **and 45 °C for sample D. The “He - Repeat” represents He permeability after injecting CO₂. The “He High Pressure”**
 150 **response is to verify testing consistency under higher pressure condition.**
 151

152 **4 Discussion**

153 The flow mechanism determines the linear or U-shaped form of the permeability curve in Fig. 5.
 154 Fracture flow, as shown in Fig. 6 (a), is the governing mechanism controlling the permeability
 155 evolution in non-sorbing He cases. The particle rearrangement by the various effective stresses
 156 reforms the particle interval (from w_0 to w_1), thus approaching the response of parallel plate flow
 157 within a fracture. In contrast, the swelling in sorbing CO₂ cases contracts the fracture cross-sectional
 158 flow area by Δb , as shown in Fig. 6 (b). The softened rock matrix results in more severe embedment
 159 and shrinks the flow path to a residual effective aperture of b_1 . The competition between effective
 160 stress and swelling dominates the U-shaped curve in Fig. 5. Fig. 6 (c) shows embedment for repeated
 161 He replacement after injection of CO₂. We quantitatively distinguish swelling and embedment by
 162 contrast calculations (between line 1, 2 and 3) based on the assumption that swelling is reversible and
 163 embedment is irreversible.
 164



165
 166 **Fig. 6. Schematic of the flowing mechanisms for a propped fracture in shale. (a) initial non-sorbing case; (b) sorbing**
 167 **case; (c) repeated non-sorbing case after injection of sorbing gas.**

168 **4.1 Quantification of embedment**

169 For steady parallel plate flow in fractures separated by a constant aperture, the evolution of
 170 fracture permeability follows the evolution of fracture aperture (Elsworth & Goodman, 1986; J. Liu,
 171 Elsworth, & Brady, 1997; Piggott & Elsworth, 1993). The permeability is proportional to the third
 172 power of fracture aperture

173

$$\frac{K_0}{K_1} = \left(\frac{b_0}{b_1}\right)^3 \quad (3)$$

174 where K_0 is the initial permeability; K_1 is the diminished permeability; b_0 is the initial aperture; and b_1
 175 is the residual aperture.

176 Experiments on fractures in granite (neither embedment nor swelling occurs) are used as a
 177 reference, in which the aperture ($b_{Granite}$) is equal to the monolayer proppant diameter (the particle
 178 deformation is negligible). Then, the residual aperture ($b_{He-shale}$) after embedment for the non-swelling
 179 and embedment-only (He) case is calculated from the relative apertures recovered from Eq. 3 for the
 180 non-embedment ($b_{Granite}$) and embedment ($b_{He-shale}$) cases, as,

$$181 \quad b_{He-shale} = b_{Granite} \sqrt[3]{\frac{K_{He-shale}}{K_{Granite}}} \quad (4)$$

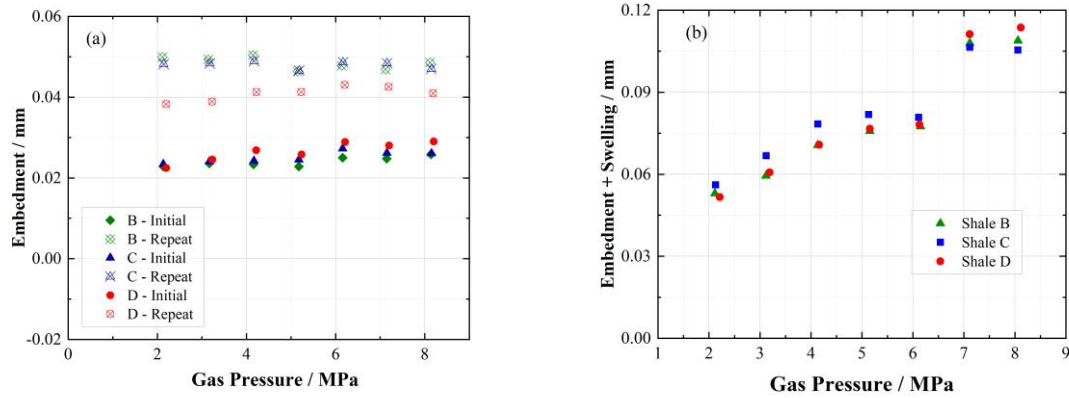
182 The embedment depth ($((b_0-b_1)/2$ in Fig. 6 (a)) is obtained from

$$183 \quad Embedment = \frac{(b_{Granite} - b_{He-shale})}{2} \quad (5)$$

184 Similarly, the aperture change for CO₂ includes the additive effects of embedment and swelling,
 185 and is evaluated from,

$$186 \quad \begin{cases} b_{CO_2-shale} = b_{Granite} \sqrt[3]{\frac{K_{CO_2-shale}}{K_{Granite}}} \\ Embedment + Swelling = \frac{(b_{Granite} - b_{CO_2-shale})}{2} \end{cases} \quad (6)$$

187 Eqs. 4 and 6 enable embedment and swelling-penetration depths to be evaluated from the
 188 permeability measurements, alone – for the shale fractures. The embedment and swelling depths are
 189 plotted in Fig. 7. In general, the embedment and swelling depths vary between 0.02 and 0.11 mm.
 190 Similar magnitudes of embedment have been recovered from morphological measurements (Kumar et
 191 al., 2015; Li et al., 2017), reportedly in the range 0.03 to 0.09 mm. The slight discrepancy between
 192 these results from the larger range of confining pressures used in this study and the recovery of
 193 swelling, occasioned when confinement is removed.



194
195 **Fig. 7. Embedment and swelling during permeation by He and CO₂. (a) Embedment for non-swelling He; (b)**
196 **Embedment and swelling for swelling CO₂.**

197 The embedment curves for He are near constant with gas pressure and fluctuate only within a
198 small range since embedment is irreversible. The gas pressure only slightly affects the permeability by
199 particle rearrangement under various effective stresses. The high repeatability of the embedment
200 results are shown for both He and CO₂ cases. The gap between the initial and repeat He tests, with
201 averaged values of 0.025 mm and 0.048mm, results from irrecoverable embedment induced by
202 swelling after the injection of CO₂ (the difference between line 1 and line 2 in Fig. 6 (a) and (c)). This
203 phenomenon is the least in Shale D test with an average repeat embedment value of 0.041 mm, where
204 the CO₂ is supercritical. In this case, sorption of CO₂ dominates over embedment, which is influenced
205 by the gas pressure following Langmuir adsorption. The embedment depth scales linearly with gas
206 pressure, as shown in Fig. 7 (b). With the addition of swelling, the aperture reduces 0.053 to 0.108
207 mm $((b_0 - b_1)/2)$ in Fig. 6 (b) as a result of injection of CO₂.

208 **4.2 Swelling analysis accommodating the Langmuir equation**

209 We quantitatively distinguish between embedment and swelling by contrasting response for these
210 two cases – embedment with He and the additive effects of embedment and swelling with CO₂.
211 Swelling-related embedment depth (Δb as shown in Fig. 6 (b)) is equal to the difference in aperture
212 reduction between CO₂ and the repeat He tests (the difference between line 2 and line 3 in Fig. 6 (b)
213 and (c)), according to the assumption that swelling is reversible and embedment is irreversible. Thus,

$$214 \text{ Swelling} = (\text{Embedment} + \text{Swelling})_{\text{CO}_2} - \text{Embedment}_{\text{He-repeat}} \quad (7)$$

215 then, the fractional adsorption may be calculated from the Langmuir isothermal adsorption relation
 216 that defines swelling-related embedment. The Langmuir relation is,

$$217 \quad \omega = \frac{V}{V_L} = \frac{P}{P_L + P} \quad (8)$$

218 where ω is the fractional adsorption; V is the adsorbed volume; V_L is the Langmuir volume; P is the
 219 injection pressure; P_L is the Langmuir pressure and is 2.5 MPa under the experimental conditions of
 220 this study.

221 Embedment for the case of He is calibrated independently from the particle deformation. The
 222 deformation γ is calculated for an elastic model as (Kewen Li, 2015; White, Jordan, Spowart, &
 223 Thadhani, 2019).

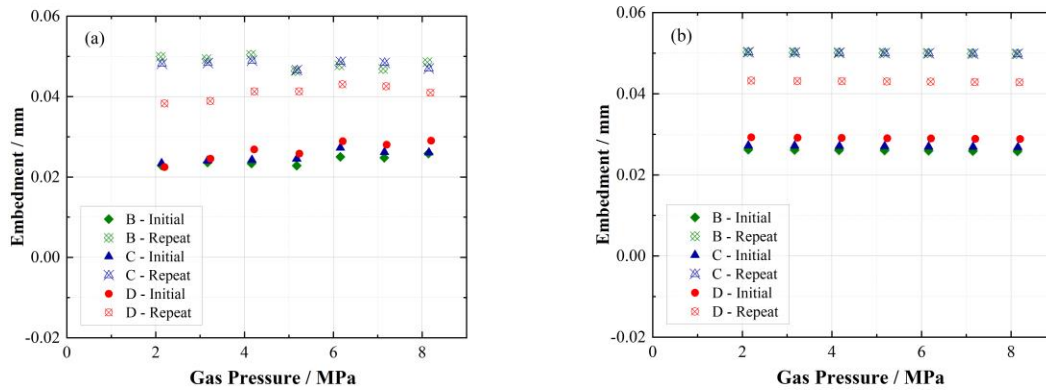
$$224 \quad \gamma = 1.04D(m^2P_{eff} \frac{1-\nu^2}{E})^{2/3} \quad (9)$$

225 where γ is the vertical deformation (“c” direction in Fig. 6 (a)); D is the particle diameter; m is the
 226 particle interval coefficient ($m=1$ when particles are uniformly displaced); P_{eff} is effective pressure
 227 applied to the particle; ν and E are Poisson Ratio and Young’s Modulus of the particle. Selected
 228 parameter values and units are shown in Table 2.

229 **Table 2. Calculation parameters and values.**

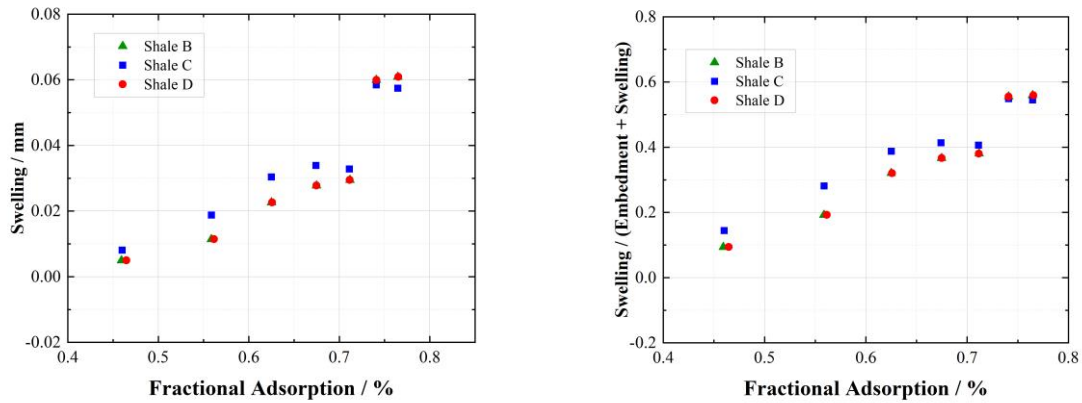
D / mm	m	ν	E / GPa
0.2884	1	0.2	34.47

230 Correcting for the reduction in proppant diameter γ due to applied stress, yields a corrected final
 231 magnitude of embedment (Fig. 8). This effect of proppant deformation is of the order of 0.001 mm
 232 and is two orders of magnitude less than the embedment for CO₂. We use this calibration to improve
 233 accuracy.



234
235 **Fig. 8. Embedment relative to gas pressure for He. (a) Original data; (b) Proppant deformation calibrated data.**

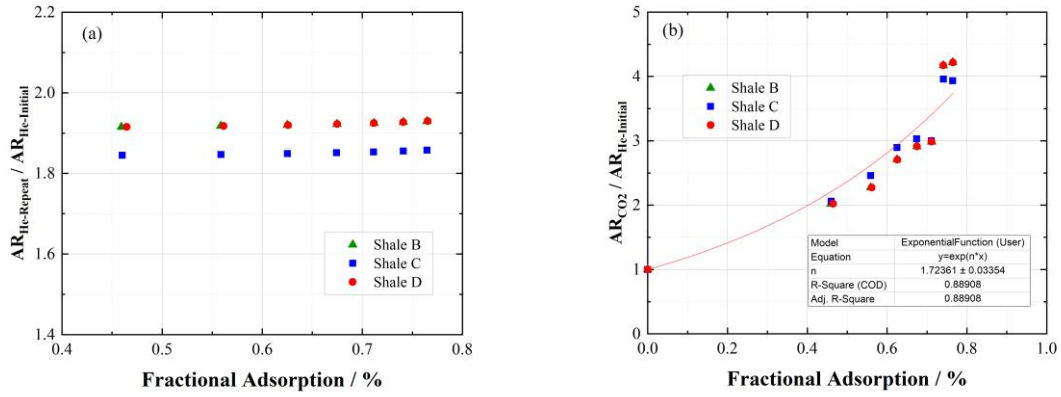
236 The swelling, its proportion and corresponding fractional adsorption are calculated by Eq. 7 and
237 Eq. 8, and plotted in Fig. 9. In general, relatively good repeatability of the measurement is
238 demonstrated by similar results recovered from the three groups of experiments. Swelling is
239 approximately proportional to the fractional adsorption (Figure 9) and ranges from 0.005 to 0.06 mm
240 and contributes 9 to 56 % of the total aperture reduction – indicating a significant effect on
241 permeability evolution.



242
243 **Fig. 9. Evolution of swelling and its proportion relative to fractional adsorption for CO₂.**

244 **4.3 Calibration equation representing swelling and induced embedment**

245 More common outcomes are generated by fitting the relation between aperture reduction ratio and
246 fractional adsorption. Aperture reduction (AR) is defined as half of the aperture change $((b_0 - b_1)/2$ as
247 shown in Fig. 6), due to both embedment and swelling. This is evaluated from Eq. 5 for the case of
248 non-sorbing He and from Eq. 6 for sorbing CO₂.



249
250 **Fig. 10. Aperture reduction (AR) ratio between initial and repeat applications of gas versus fractional adsorption for**
251 **(a) He and for (b) CO₂.**

252 As shown in Fig. 10 (a), swelling increases embedment by a factor of 1.84 to 1.93 between the He
253 permeability experiments. For CO₂, a power-law relation is apparent between fractional adsorption
254 and aperture reduction (Fig. 10 (b)) as conditioned by the choice of Eq. 6. The aperture reduction ratio
255 is unity when fractional adsorption is zero, as implied by the absence of swelling. By fixing this
256 intercept (the Point (0, 1) in Fig. 10 (b)), the aperture reduction can be calibrated to the empirical
257 equation,

$$258 \quad \frac{AR_1}{AR_0} = e^{1.724\omega} = e^{1.724 \frac{P}{P_L + P}} \quad (10)$$

259 where the AR_1 is the calibrated aperture reduction $((b_0 - b_1)/2)$ as shown in Fig. 6 (b) involving both
260 embedment and swelling and AR_0 is the initial aperture reduction $((b_0 - b_1)/2)$ as shown in Fig. 6 (a)
261 neglecting the swelling effect. The value of AR_1 accommodates the swelling effect and updates the
262 prediction of the permeability in propped fractures.

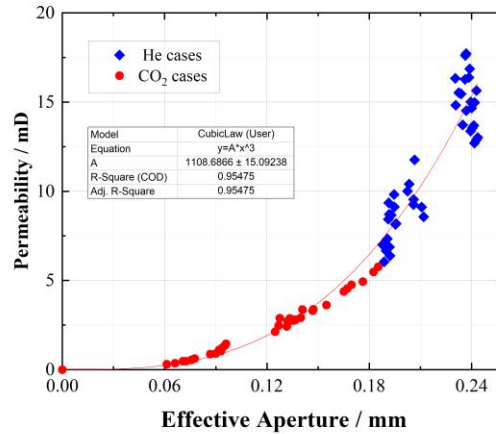
263 4.4 Verification

264 An indirect method is proposed to examine the universal applicability of Eq. 10 – since few direct
265 measurements of embedment and swelling are available. Permeability is the target parameter for the
266 verification. The correlation between effective aperture and permeability is simplified to a cubic
267 power-law relation as

$$268 \quad K = \theta b_{eff}^3 \quad (11)$$

269 where θ is the coefficient of the aperture-permeability correlation and is obtained through trial and
270 error; b_{eff} is the effective aperture and is an intermediate variable calculated from Eq. 3.

271 In this study, we fit the cubic relation between permeability and effective aperture in Fig. 11. A
 272 user-defined model ($y=Ax^3$) is used for regression based on the definition of fluid flow cross-sectional
 273 area (A) in Eq. 1, where flow in the rock matrix is ignored. The fitted coefficient (θ) is 1109, which
 274 can be used as a reference or comparison for trial and error verification.



275 **Fig. 11. The cubic power-law relation fit to permeability versus effective aperture for all cases.**

276 Then, the non-sorbing gas permeability is applied to predict the permeability for the sorbing gas
 277 case by the following relations,
 278

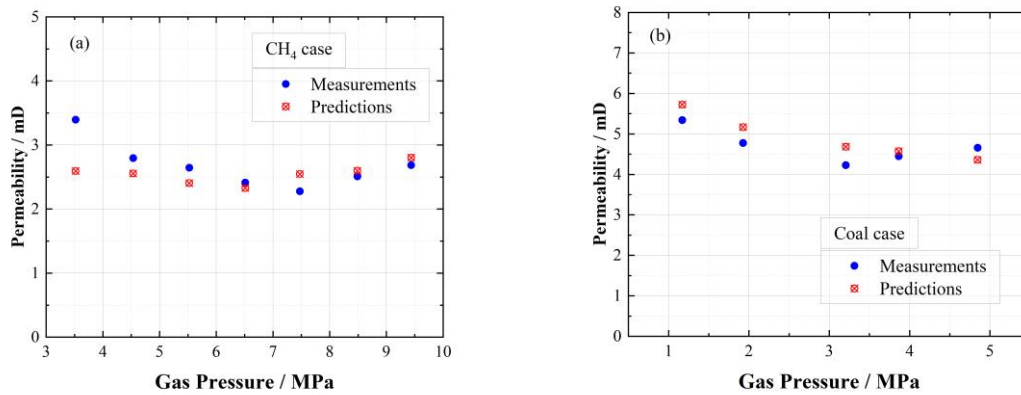
$$279 \quad AR = (D - b_{eff}) / 2 = (D - \sqrt[3]{\frac{K}{\theta}}) / 2 \quad (12)$$

$$280 \quad \frac{AR_1}{AR_0} = \frac{\theta D - \sqrt[3]{\theta^2 K_1}}{\theta D - \sqrt[3]{\theta^2 K_0}} = e^{1.724 \frac{P}{P_L + P}} \quad (13)$$

281 where D is the average particle diameter; K_1 is the predicted permeability for the case of sorbing gas;
 282 K_0 is the measured permeability for the case of non-sorbing gas, recovered from the corresponding
 283 series of experiments.

284 Prior experimental results are available with different rock types and for different gases (Kumar et
 285 al., 2015; Li et al., 2017), including coal (with injection of CO_2) and CH_4 (in a propped shale sample).
 286 For coal, 70 ~ 140 mesh proppant was used, with an average diameter of 0.159 mm and a Langmuir
 287 pressure of ~1.75 MPa. For shale with CH_4 , the corresponding average diameter and Langmuir
 288 pressure are 0.288 mm and 3.5 MPa, respectively. The optimized coefficients (θ) obtained by trial and
 289 error, are 280 for CH_4 (shale) and 2250 for coal (CO_2), respectively, with results shown in Fig. 12.
 290 Apparently, the predictions fit the measurements and exhibit similar trends with gas pressure. The

291 MRD (mean relative deviation) and MAD (mean absolute deviation) are -3.57 % and 9.22 % for the
 292 prediction for CH₄ in shale and -4.50 % and 7.06 % for CO₂ in coal.



293
 294 **Fig. 12. Permeability prediction and comparison for (a) CH₄ case and (b) Coal case.**

295 **5 Conclusions**

296 Permeability evolution in propped shale fractures to non-adsorptive He and adsorptive CO₂ have
 297 been measured. Embedment and swelling depth have been evaluated by using rigid split samples of
 298 granite as an example where no embedment can occur. Further analyses have included comparisons
 299 between non-adsorptive gases and adsorptive gas utilizing the Langmuir isotherm to define swelling
 300 and embedment effects. The main observations of this work are as follow:

301 (1) Permeability evolution is linear with pressure for non-sorbing He, U-shaped for sorbing CO₂
 302 (gaseous) and W-shaped curve for supercritical CO₂. One exception is for liquid CO₂, which forms a
 303 linear curve with the lowest permeability. The competition between injection pressure (changing the
 304 effective stress) and swelling and the phase state transformation are the main factors controlling these
 305 forms of permeability evolution for the case of CO₂.

306 (2) Permeability evolution is linear in pressure for both initial and repeated He injection, with the
 307 intervening injection of CO₂ – but parallel and offset. Approximately ~50-70 % of the permeability
 308 recovers from the recovery of swelling after the desorption of CO₂, in which supercritical CO₂
 309 increases the permeability recovery by ~20% when compared with the case for gaseous CO₂.

310 (3) Embedment depth is 0.025 to 0.048 mm for permeation of He, while swelling increases the
 311 embedment by a factor of ~1.84-1.93 between the initial and repeated He tests. The swelling and
 312 induced embedment, for CO₂, varies between 0.053 and 0.108 mm where the swelling depth

313 contributes 0.005 to 0.06 mm, representing 9 to 56 % of the total aperture reduction relative to the
314 adsorbed mass. These depths are approximately proportional to the gas pressure and fractional
315 adsorption for the case of CO₂, and near constant for He.

316 (4) A new calibration equation representing swelling and induced embedment is generated
317 accommodating Langmuir isothermal sorption and verified against prior experiments with different
318 rock types (coal) and for different sorbing gases (CH₄). It provides an improved method for predicting
319 fracture conductivity related to enhanced gas recovery, and also benefits the understanding of CO₂
320 sealing behaviour and long-term migration, thus improving the evaluation of CO₂ storage capacity
321 and security.

322

323 **Acknowledgements**



324

325 This research has received funding from the European Union's Horizon 2020 research and
326 innovation programme under the Marie Skłodowska-Curie grant agreement No. 846775.

327

328 **References**

- 329 Arshadi, M., Zolfaghari, A., Piri, M., Al-Muntasheri, G. A., & Sayed, M. (2017). The effect of deformation on
330 two-phase flow through proppant-packed fractured shale samples: A micro-scale experimental
331 investigation. *Advances in Water Resources*, *105*, 108-131. doi:10.1016/j.advwatres.2017.04.022
- 332 Bandara, K. M. A. S., Ranjith, P. G., & Rathnaweera, T. D. (2019). Improved understanding of proppant
333 embedment behavior under reservoir conditions: A review study. *Powder Technology*, *352*, 170-192.
334 doi:10.1016/j.powtec.2019.04.033
- 335 Bielicki, J. M., Langenfeld, J. K., Tao, Z., Middleton, R. S., Menefee, A. H., & Clarens, A. F. (2018). The
336 geospatial and economic viability of CO₂ storage in hydrocarbon depleted fractured shale formations.
337 *International Journal of Greenhouse Gas Control*, *75*, 8-23. doi:10.1016/j.ijggc.2018.05.015
- 338 Brace, W. F., Walsh, J. B., & Frangos, W. T. (1968). Permeability of granite under high pressure. *Journal of*
339 *Geophysical Research*, *73*(6), 2225-2236. doi:10.1029/JB073i006p02225
- 340 Buscheck, T. A., White, J. A., Carroll, S. A., Bielicki, J. M., & Aines, R. D. (2016). Managing geologic CO₂
341 storage with pre-injection brine production: a strategy evaluated with a model of CO₂ injection at Snøhvit.
342 *Energy & Environmental Science*, *9*(4), 1504-1512. doi:10.1039/c5ee03648h
- 343 Elsworth, D., & Goodman, R. E. (1986). Characterization of rock fissure hydraulic conductivity using idealized
344 wall roughness profiles. *International Journal of Rock Mechanics and Mining Sciences & Geomechanics*
345 *Abstracts*, *23*(3), 233-243.
- 346 Gale, J. F. W., Laubach, S. E., Olson, J. E., Eichhuble, P., & Fall, A. (2014). Natural Fractures in shale: A
347 review and new observations. *AAPG Bulletin*, *98*(11), 2165-2216. doi:10.1306/08121413151
- 348 Hoek, E., & Martin, C. D. (2014). Fracture initiation and propagation in intact rock – A review. *Journal of Rock*
349 *Mechanics and Geotechnical Engineering*, *6*(4), 287-300. doi:10.1016/j.jrmge.2014.06.001
- 350 Kewen Li, Y. G., Youchang Lyu. (2015). New mathematical models for calculating proppant embedment and
351 fracture conductivity. *SPE Journal*, *20*(03), 1-12.
- 352 Kolster, C., Masnadi, M. S., Krevor, S., Mac Dowell, N., & Brandt, A. R. (2017). CO₂ enhanced oil recovery: a
353 catalyst for gigatonne-scale carbon capture and storage deployment? *Energy & Environmental Science*,
354 *10*(12), 2594-2608. doi:10.1039/c7ee02102j
- 355 Kumar, H., Elsworth, D., Liu, J., Pone, D., & Mathews, J. P. (2015). Permeability evolution of propped artificial
356 fractures in coal on injection of CO₂. *Journal of Petroleum Science and Engineering*, *133*, 695-704.
357 doi:10.1016/j.petrol.2015.07.008
- 358 Li, X., Feng, Z., Han, G., Elsworth, D., Marone, C., Saffer, D., & Cheon, D.-S. (2017). Permeability Evolution
359 of Propped Artificial Fractures in Green River Shale. *Rock Mechanics and Rock Engineering*, *50*(6), 1473-
360 1485. doi:10.1007/s00603-017-1186-2
- 361 Liu, H.-H., & Rutqvist, J. (2009). A New Coal-Permeability Model: Internal Swelling Stress and Fracture–
362 Matrix Interaction. *Transport in Porous Media*, *82*(1), 157-171. doi:10.1007/s11242-009-9442-x
- 363 Liu, H., Wang, F., Zhang, J., Meng, S., & Duan, Y. (2014). Fracturing with carbon dioxide: Application status
364 and development trend. *Petroleum Exploration and Development*, *41*(4), 513-519. doi:10.1016/s1876-
365 3804(14)60060-4

366 Liu, J., Elsworth, D., & Brady, B. H. (1997). Analytical evaluation of post-excavation hydraulic conductivity
367 field around a tunnel. *International Journal of Rock Mechanics and Mining Sciences*, 23(3-4), 181.e181-
368 181.e187.

369 Mazumder, S., & Wolf, K. H. (2008). Differential swelling and permeability change of coal in response to CO₂
370 injection for ECBM. *International Journal of Coal Geology*, 74(2), 123-138.
371 doi:10.1016/j.coal.2007.11.001

372 Middleton, R. S., Carey, J. W., Currier, R. P., Hyman, J. D., Kang, Q., Karra, S., . . . Viswanathan, H. S. (2015).
373 Shale gas and non-aqueous fracturing fluids: Opportunities and challenges for supercritical CO₂. *Applied*
374 *Energy*, 147, 500-509. doi:10.1016/j.apenergy.2015.03.023

375 Piggott, A. R., & Elsworth, D. (1993). Laboratory assessment of the equivalent apertures of a rock fracture.
376 *GEOPHYSICAL RESEARCH LETTERS*, 20(13), 1387-1390.

377 Santos, L., Dahi Taleghani, A., & Li, G. (2018). Expandable proppants to moderate production drop in
378 hydraulically fractured wells. *Journal of Natural Gas Science and Engineering*, 55, 182-190.
379 doi:10.1016/j.jngse.2018.04.026

380 Tang, Y., & Ranjith, P. G. (2018). An experimental and analytical study of the effects of shear displacement,
381 fluid type, joint roughness, shear strength, friction angle and dilation angle on proppant embedment
382 development in tight gas sandstone reservoirs. *International Journal of Rock Mechanics and Mining*
383 *Sciences*, 107, 94-109. doi:10.1016/j.ijrmms.2018.03.008

384 Tayari, F., & Blumsack, S. (2020). A real options approach to production and injection timing under uncertainty
385 for CO₂ sequestration in depleted shale gas reservoirs. *Applied Energy*, 263.
386 doi:10.1016/j.apenergy.2020.114491

387 Wang, S., Elsworth, D., & Liu, J. (2011). Permeability evolution in fractured coal: The roles of fracture
388 geometry and water-content. *International Journal of Coal Geology*, 87(1), 13-25.
389 doi:10.1016/j.coal.2011.04.009

390 Wang, S., Elsworth, D., & Liu, J. (2013). Permeability evolution during progressive deformation of intact coal
391 and implications for instability in underground coal seams. *International Journal of Rock Mechanics and*
392 *Mining Sciences*, 58, 34-45. doi:10.1016/j.ijrmms.2012.09.005

393 Wang, S., Feng, Q., Javadpour, F., Xia, T., & Li, Z. (2015). Oil adsorption in shale nanopores and its effect on
394 recoverable oil-in-place. *International Journal of Coal Geology*, 147-148, 9-24.
395 doi:10.1016/j.coal.2015.06.002

396 Wen, Q., Zhang, S., Wang, L., Liu, Y., & Li, X. (2007). The effect of proppant embedment upon the long-term
397 conductivity of fractures. *Journal of Petroleum Science and Engineering*, 55(3-4), 221-227.
398 doi:10.1016/j.petrol.2006.08.010

399 Weng, X. (2015). Modeling of complex hydraulic fractures in naturally fractured formation. *Journal of*
400 *Unconventional Oil and Gas Resources*, 9, 114-135. doi:10.1016/j.juogr.2014.07.001

401 White, B. W., Jordan, J. L., Spowart, J. E., & Thadhani, N. N. (2019). Particle strain analysis of epoxy-based
402 composites following quasi-static and dynamic compression. *Journal of Dynamic Behavior of Materials*,
403 5(1), 24-38. doi:10.1007/s40870-019-00182-2

404 Zhang, J., & Hou, J. (2016). Theoretical conductivity analysis of surface modification agent treated proppant II
405 – Channel fracturing application. *Fuel*, 165, 28-32. doi:10.1016/j.fuel.2015.10.026

406 Zhang, J., Ouyang, L., Zhu, D., & Hill, A. D. (2015). Experimental and numerical studies of reduced fracture
407 conductivity due to proppant embedment in the shale reservoir. *Journal of Petroleum Science and*
408 *Engineering*, 130, 37-45. doi:10.1016/j.petrol.2015.04.004
409 Zhang, X., Lu, Y., Tang, J., Zhou, Z., & Liao, Y. (2017). Experimental study on fracture initiation and
410 propagation in shale using supercritical carbon dioxide fracturing. *Fuel*, 190, 370-378.
411 doi:10.1016/j.fuel.2016.10.120
412 Zhang, X., Ranjith, P. G., Lu, Y., & Ranathunga, A. S. (2019). Experimental investigation of the influence of
413 CO₂ and water adsorption on mechanics of coal under confining pressure. *International Journal of Coal*
414 *Geology*, 209, 117-129. doi:10.1016/j.coal.2019.04.004
415 Zhi, S., Elsworth, D., & Liu, L. (2019). W-shaped permeability evolution of coal with supercritical CO₂ phase
416 transition. *International Journal of Coal Geology*, 211, 1-14. doi:10.1016/j.coal.2019.103221
417